Structure
Article

A Self-Sequestered Calmodulin-like Ca^{2+} Sensor of Mitochondrial SCaMC Carrier and Its Implication to Ca^{2+}-Dependent ATP-Mg/P_i Transport

Qin Yang,[1] Sven Brüschweiler,[1] and James J. Chou[1,*]
[1]Department of Biological Chemistry and Molecular Pharmacology, Harvard Medical School, Boston, MA 02115, USA
*Correspondence: chou@cmcd.hms.harvard.edu
http://dx.doi.org/10.1016/j.str.2013.10.018

SUMMARY

The mitochondrial carriers play essential roles in energy metabolism. The short Ca^{2+}-binding mitochondrial carrier (SCaMC) transports ATP-Mg in exchange for P_i and is important for activities that depend on adenine nucleotides. SCaMC adopts, in addition to the transmembrane domain (TMD) that transports solutes, an extramembrane N-terminal domain (NTD) that regulates solute transport in a Ca^{2+}-dependent manner. Crystal structure of the Ca^{2+}-bound NTD reveals a compact architecture in which the functional EF hands are sequestered by an endogenous helical segment. Nuclear magnetic resonance (NMR) relaxation rates indicated that removal of Ca^{2+} from NTD results in a major conformational switch from the rigid and compact Ca^{2+}-bound state to the dynamic and loose apo state. Finally, we showed using surface plasmon resonance and NMR titration experiments that free apo NTDs could specifically interact with liposome-incorporated TMD, but that Ca^{2+} binding drastically weakened the interaction. Our results together provide a molecular explanation for Ca^{2+}-dependent ATP-Mg flux in mitochondria.

INTRODUCTION

Mitochondrial matrices house essential components of energy metabolism in cell. Since the matrices are closed compartments, linking biochemical pathways of mitochondria and cytosol requires selective trafficking of metabolites, nucleotides, inorganic phosphates, and vitamins across the mitochondrial inner membrane, and these transport activities are mediated by a large family of membrane proteins on the inner membrane, collectively termed mitochondrial carriers (Klingenberg, 2009; Palmieri et al., 2006; Walker and Runswick, 1993). Mitochondrial carriers adopt a range of transport modes including uniport, symport, and antiport; their transport activities are driven by substrate concentration gradient and membrane potential across the inner membrane (Dehez et al., 2008; Kunji and Robinson, 2010; Palmieri et al., 2011). The structures of two family members have been characterized. The crystal structures of the ADP/ATP carrier (AAC; Kunji and Harding, 2003; Pebay-Peyroula et al., 2003) and the nuclear magnetic resonance (NMR) structure of the uncoupling protein 2 (UCP2; Berardi et al., 2011) all show an open-top container architecture formed with three structurally similar domains, and each domain consists of two packed transmembrane helices separated in sequence by an amphipathic helix. Based on sequence homology within the mitochondrial carrier family, other members are believed to have similar structural scaffolds (Palmieri et al., 2011).

There is, however, an unusual mitochondrial carrier that adopts, in addition to the transmembrane domain (TMD), an N-terminal domain (NTD) with Ca^{2+} binding signatures that extends beyond the membrane into the intermembrane space. This protein is the short Ca^{2+}-binding mitochondrial carrier (SCaMC) that transports ATP-Mg in exchange for P_i and thereby modulates the matrix adenine nucleotide content (Satrústegui et al., 2007; Traba et al., 2011). SCaMC is one of the two carriers responsible for transporting ATP. Although AAC accounts for the bulk ADP/ATP recycling in the matrix by exporting newly synthesized ATP out of the matrix while importing ADP for continuous synthesis (Traba et al., 2009b), the transport activity of SCaMC is important for mitochondrial activities that depend on adenine nucleotides, such as gluconeogenesis, mitochondrial biogenesis, and mitochondrial DNA maintenance (Amigo et al., 2013; Cavero et al., 2005; Chen et al., 2011; Kucejova et al., 2008; Llorente-Folch et al., 2013; Satrústegui et al., 2007). SCaMC is abundant and, to date, five major paralogs have been identified: *SCaMC-1/SLC25A24*, *SCaMC-2/SLC25A25*, *SCaMC-3/SLC25A23* (Bassi et al., 2005; del Arco and Satrústegui, 2004; Fiermonte et al., 2004; Mashima et al., 2003), *SCaMC-1L* (Amigo et al., 2012), and *SCaMC-3L* (Traba et al., 2009a), most of which have several alternative spliced variants (del Arco and Satrústegui, 2004). The major difference between SCaMC and AAC is the specific regulation of only SCaMC by Ca^{2+}. Studies in isolated hepatocytes and mitochondria have reported that SCaMC remains inactive, unless stimulated by a cytosolic Ca^{2+} signal (Amigo et al., 2013; Chen, 2004; Dransfield and Aprille, 1993; Hagen et al., 1993; Nosek et al., 1990; Traba et al., 2012). The finding is consistent with SCaMC having a characteristic Ca^{2+} binding domain (Satrústegui et al., 2007).

It has been difficult to elucidate the role of the NTD in Ca^{2+}-dependent transport activity because we have not seen a structural example illustrating how membrane transporter can be regulated by a covalently tethered ectodomain. Therefore, it is of fundamental interest to investigate the role of the SCaMC NTD in sensing Ca^{2+} and in interacting with the

substrate-transporting TMD. Based on sequence analysis, the NTD contains four EF-hand motifs in a calmodulin-like (CaM-like) arrangement, i.e., the N- and C-terminal lobes each consist of two EF hands with two Ca^{2+} binding loops (Hoeflich and Ikura, 2002). CaM is a ubiquitous Ca^{2+} sensor that is essential for numerous cellular Ca^{2+}-regulated signaling pathways, including the function of several ion channels (Clapham, 2007; Van Petegem et al., 2005; Wingo et al., 2004). The overall Ca^{2+}-triggered conformational switch is well understood for CaM. In the absence of Ca^{2+}, four helices from two EF hands in each of the N- and C-lobes fold into a compact four-helix bundle in which hydrophobic residues of the helices are buried inside a hydrophobic core (Kuboniwa et al., 1995; Tjandra et al., 1995). Upon Ca^{2+} coordination by the Ca^{2+} binding loops, the EF-hand helices open up, exposing the hydrophobic residues (Chou et al., 2001). This conformational switch allows the EF hands to clamp onto their target peptides, as in the case of Ca^{2+}-dependent activation of the myosin light-chain kinase by CaM during muscle contraction (Ikura et al., 1992; Meador et al., 1992). In CaM, there is also a flexible linker connecting the N- and C-lobes, which permits the two domains to wrap around the same peptide (Barbato et al., 1992).

Although the SCaMC NTD also has four EF hands, there does not appear to be a flexible central linker between the N- and C-lobes according to secondary structure prediction (del Arco and Satrústegui, 2004), and sequence analysis also predicted an additional C-terminal helix (Figure S1 available online). These predicted differences raised the question of whether the NTD adopts a Ca^{2+}-dependent mode of action different from that of CaM. Moreover, it is still not clear whether the NTD interacts at all with the TMD.

In this study, we used a combination of X-ray crystallography, NMR, and surface plasmon resonance (SPR) approaches to investigate Ca^{2+}-triggered structural changes of human SCaMC-1 NTD and its interaction with the TMD. We showed that the NTD can undergo change from the dynamic apo state that specifically binds to the transporter domain to a rigid and compact structure upon Ca^{2+} binding, and this conformational switch essentially abrogates interaction with the substrate-transporting TMD.

RESULTS

Structure Determination

We attempted to determine the crystal structure of the human SCaMC-1 NTD in both apo and Ca^{2+}-bound states. Although the Ca^{2+}-bound NTD could be crystallized, the apo state resisted extensive crystallization trials and was later found to be highly dynamic by NMR measurements. The Ca^{2+}-bound NTD was crystallized in two different space groups, $P6_222$ and $P3_121$. Initial phase and structural model were obtained from the 2.9 Å multiple-wavelength anomalous diffraction data collected on $P6_222$ crystals of selenomethionine-labeled protein (Doublié, 2007; Yang et al., 2011). We then used the model and solved the phase of the $P3_121$ data set by molecular replacement. The structure of the Ca^{2+}-bound NTD in the $P3_121$ crystal was subsequently refined to 2.1 Å with good statistics (R = 17.67%, R_{free} = 22.53%; full statistics in Table 1). The construct that was successfully crystallized above consisted of residues 1–193. We included residues 156–193, a region of the NTD that is between the EF-hand-rich domain and the TMD, with the intention to examine its potential interaction with the EF hands (Figure S2A). In the electron density map, however, only residues 22–176 were visible.

The Ca^{2+}-Bound NTD Has a Compact Structure with Self-Sequestered EF Hands

The crystal structure of the Ca^{2}-bound NTD shows a rigid and elongated architecture that contains three main structured regions: the N-terminal lobe (residues 22–87) and the C-terminal lobe (residues 88–152), each consisting of two Ca^{2+}-bound EF hands, and a C-terminal helix (residues 159–170) (Figure 1A). All four EF hands have the typical EF-hand conformation as seen in the Ca^{2+}-bound CaM, in which two α helices flank the canonical 12-residue Ca^{2+}-coordinating loop (Gifford et al., 2007; Figure 1A). For each Ca^{2+}-coordinating loop, the main-chain carbonyl, side-chain carboxylates, and a bridged water molecule coordinate Ca^{2+} in a 7-fold pentagonal dipyramid fashion (Figure S2B). The distances between two Ca^{2+} ions in the N- and C-lobes are 11.7 Å and 11.9 Å, respectively; they are very similar to those in other EF-hand pairs (Gifford et al., 2007).

Despite the structural similarity in the N- and C-lobes between the Ca^{2+}-bound NTD and CaM, the overall conformations are profoundly different. The Ca^{2+}-bound NTD is rigid and compact, whereas CaM adopts an extended dumbbell shape in which the N- and C-lobes are linked by a six-residue flexible linker and are free to move relative to each other in solution (Barbato et al., 1992; Taylor et al., 1991; Figure 1B). For NTD, however, the flexible linker between the two lobes essentially does not exist. Consequently, the second helix of EF hand II (H4) and the first helix of EF hand III (H5) merge into a continuous central helix that bridges the N- and C-lobes (Figure 1A). Unlike CaM, this central helix is short enough to allow the N- and C-lobes to be positioned in proximity to form extensive hydrogen bonds and nonpolar contacts. Main interactions are those between the intervening loop (residues 51–59) connecting EF hands I and II of N-lobe and the loop (residues 152–159) C-terminal to EF hand IV of C-lobe (Figure 1A). These interactions bury an interface of about 726 $Å^2$, which accounts for more than 13% of the surface of the individual lobes. These interlobe contacts effectively lock the four EF hands in a compact fold while stabilizing the central helix.

Another unusual and important feature of the NTD is the C-terminal helix (H9) in addition to the four EF hands. This helix encompasses a conserved sequence (residues 159–168) and forms extensive nonpolar interactions with the hydrophobic clamps of EF hands III and IV (Figures 2A, 2B, and S3). Hydrophobic clamps of EF hands are binding sites for target peptides in CaM (Gifford et al., 2007). Indeed, the H9 in complex with the C-lobe in NTD aligns well with target peptide in several CaM-peptide complexes (Figure 2C; Hoeflich and Ikura, 2002), suggesting that it serves as an internal target peptide for the NTD EF hands, similar to the sterile α motif of the stromal interaction molecule (STIM; Stathopulos et al., 2008; Zheng et al., 2011).

Due to the earlier example in which crystal packing caused the flexible central linker in the Ca^{2+}-bound CaM to be helical, we

Table 1. Data Collection and Refinement Statistics

PDB ID code	SeMet Peak	SeMet Inflection	SeMet Remote	Native 4N5X
Data collection				
Wavelength (Å)	0.9794	0.9795	0.9494	1.5418
Resolution (Å)	40–2.9 (2.98–2.9)[a]	40–2.92 (3.03–2.92)	40–3.0 (3.1–3.0)	20–2.1 (2.17–2.10)
Space group	$P6_222$	$P6_222$	$P6_222$	$P3_121$
Cell dimensions				
a = *b* (Å)	74.480	74.489	74.503	51.210
c (Å)	173.637	173.650	173.709	112.153
α = β (°)	90	90	90	90
γ (°)	120	120	120	120
Total reflections	260,454 (20,594)	254,334 (28,333)	235,619 (23,782)	111,675 (10,536)
Unique reflections	11,865 (886)	11,613 (1,220)	10,726 (1,023)	10,443 (1,013)
Redundancy	21.6 (23.2)	21.9 (23.2)	21.9 (23.2)	10.6 (10.4)
$I/\sigma I$	26.89 (5.09)	27.95 (5.74)	27.22 (5.69)	21.96 (6.18)
Completeness (%)	99.1 (100)	99.0 (100)	99.2 (100)	100 (99.9)
R_{merge} (%)	8 (90.8)	7.9 (80.7)	8.1 (86.5)	10.7 (40.0)
Phasing				
No. of SeMet sites	4			
Figure of merit (AutoSol)	0.58			
Refinement				
Resolution (Å)				20–2.10
No. reflections				10,443
R_{work}/R_{free} (%)[b]				17.67/22.53[c]
Root-mean-square deviations				
Bond lengths (Å)				0.007
Bond angles (°)				1.151
B-factors (Å^2)				
SCaMC (chain A)				22.762
Ca^{2+} (chain B)				18.742
Water				26.939
Ramachandran plot statistics (%)				
Most favored regions				99.34
Allowed regions				0.66
Disallowed regions				0

SeMet, selenomethionine.
[a]Values in parentheses are for the highest-resolution shell.
[b]R_{work} and $R_{free} = S_h ||F_o| - |F_c|| / S_h |F_o|$, where F_o and F_c are the observed and calculated structure factor amplitudes. R_{free} was calculated with ~5% of the reflections not used in refinement.
[c]$R_{merge} = S |I - \langle I \rangle| / S I$, where <I> is the average intensity from multiple observations of symmetry-related reflections.

had the concern that crystal contacts also could have artificially stabilized the compact state of SCaMC-1 NTD. Thus, we examined the structure of the Ca^{2+}-bound NTD in solution. We measured the ^1H-^{15}N residual dipolar coupling (RDC) $^1D_{NH}$ for Ca^{2+}-bound NTD in a liquid crystalline medium composed of filamentous phage (Pf1). The measured $^1D_{NH}$ fitted the crystal structure well with Pearson correlation coefficient (*R*) of 0.945 and quality factor (*Q*) of 27.8% (Figure 1C). The seven outliers with discrepancy larger than 10 Hz (e.g., residues 41, 58, and 137) are located in the loop regions and at the beginnings of helices (Figure 1C). The RDC data confirmed that the Ca^{2+}-bound NTD in solution adopts the same structure as in crystal.

The apo NTD Is Distinctly More Dynamic and Less Structured

To investigate potential Ca^{2+}-triggered conformational change of SCaMC-1 NTD, we measured structural properties of the NTD in the absence of Ca^{2+} by NMR (Figure 3). We attempted to crystallize the apo NTD but were not successful. We then found, during measurements of NMR relaxation rates, that the apo NTD has very substantial internal dynamics, which explains the unsuccessful crystallization trials. The ^1H-^{15}N transverse relaxation optimized spectroscopy-heteronuclear single quantum coherence (TROSY-HSQC) spectra of the apo and Ca^{2+}-bound NTD are completely different (Figure S4A), indicating

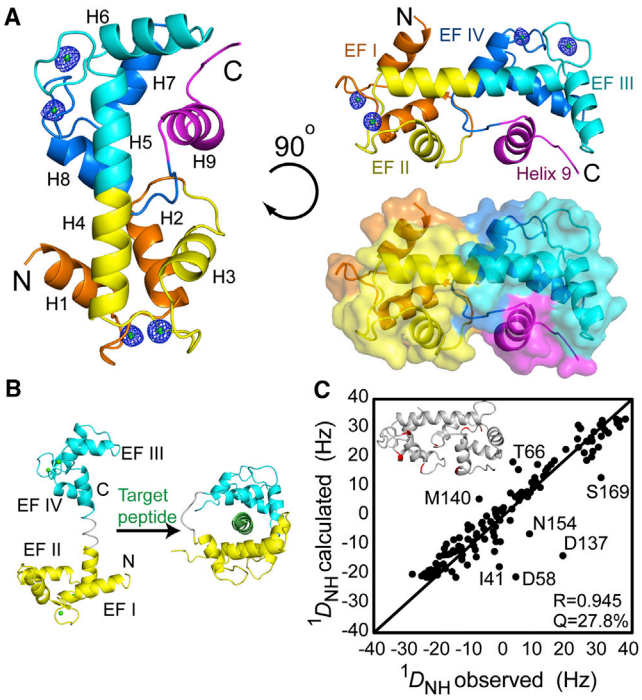

Figure 1. Structure of the Ca^{2+}-Bound NTD of Human SCaMC-1 Shows a Self-Sequestered CaM-like Architecture

(A) Cartoon and surface representations of the 2.1 Å crystal structure of the Ca^{2+}-bound NTD. The NTD construct used for structure determination consists of residues 1–193, but electron density was observed only for residues 22–173. EF hands are colored in orange, yellow, cyan, and blue. The extra helix (H9) after the CaM-like domain is colored in magenta. Ca^{2+} ions are represented by green spheres, and their simulated omit maps are shown as blue mesh (contoured at 4 σ). See also Figure S2.

(B) Structures of the Ca^{2+}-CaM with and without the bound peptide, shown for comparison with the NTD. Ca^{2+}-CaM and Ca^{2+}-CaM-peptide complexes are adapted from Protein Data Bank (PDB) ID codes 4CLN and 2BBN, respectively. The N- and C-lobes are colored in yellow and cyan, respectively. The central flexible loop is in gray and the target peptide is in green.

(C) Correlation of $^1D_{NH}$ measured for Ca^{2+}-bound NTD in solution to $^1D_{NH}$ values calculated based on the 2.1 Å crystal structure. The goodness of fit was assessed by Pearson correlation coefficient (R) and the quality factor (Q). The outliers with discrepancy between measured and calculated $^1D_{NH}$ larger than 10 Hz are mapped onto the structure of the Ca^{2+}-bound NTD (insert).

that the structural and/or dynamic properties of the two states are very different and that Ca^{2+} binding clearly triggers a major conformational switch in the protein.

We then compared the dynamic properties of the apo and Ca^{2+}-bound NTD by measuring protein backbone ^{15}N relaxation rates R_1 and R_2 and heteronuclear $^{15}N(^1H)$ nuclear Overhauser effect (NOE) for both states. The relaxation data for the Ca^{2+}-bound NTD are very uniform (except for N and C terminus; Figures 3A, 3C, and 3E), which is indicative of a rigid and compact structure where the structured segments of the protein tumble together in solution. In contrast, the relaxation rates and the heteronuclear NOE of the apo NTD are very heterogeneous (Figures 3B, 3D, and 3F). Regions that have low heteronuclear NOE values include H3 and adjacent loops (residues 50–78), the Ca^{2+}-binding loop of EF hand III (residues 99–109), as well as the C-terminal H9 (residues 159–170) (Figures 3B and 3G). In particular, heteronuclear NOEs indicate that residues 50–78, which stabilize interlobe interactions in the Ca^{2+}-bound state, are essentially disordered in the apo state (Figures 3B and 3G). In addition to the disordered regions, the heteronuclear NOEs of the structured EF hands in the apo NTD are also uniformly lower than those in the Ca^{2+}-bound NTD (Figures 3A and 3B), indicating that the structured regions that remain in the apo state are also dynamic with respect to each other. These results together show that apo NTD does not adopt a defined conformation, is loosely packed, and has a significant amount of disordered regions.

The NTD Binds Specifically to the TMD in a Ca^{2+}-Dependent Manner

The above structural characterization of SCaMC-1 NTD in the absence and presence of Ca^{2+} clearly shows the existence of Ca^{2+}-triggered conformational switch in NTD. To investigate whether NTD interacts with TMD and, if so, whether Ca^{2+} influences the interaction, we first used SPR to examine direct association of NTD to TMD in the absence and presence of Ca^{2+}. The TMD of SCaMC-1 was overexpressed, purified, and reconstituted in dodecyl-phosphocholine (DPC) micelles using a protocol similar to that used previously for another mitochondrial carrier, UCP2 (Berardi et al., 2011), and was further incorporated into 1-palmitoyl-2-oleoyl-sn-glycero-3-phosphocholine (POPC)/1-palmitoyl-2-oleoyl-sn-glycero-3-phosphoglycerol (POPG)/cardiolipin liposome while removing detergent completely. The TMD proteoliposome was then immobilized onto the L1 sensor chip (Hodnik and Anderluh, 2010; Stahelin, 2013) for studying its interaction with NTD. The SPR measurements showed that the NTD could bind specifically to TMD proteoliposome with a K_D of 250 ± 50 μM in the absence of Ca^{2+} and that the interaction is at least 20-fold lower in the presence of 5 mM Ca^{2+} (K_D = 5,600 ± 1,000 μM) (Figures 4A and 4B).The binding affinity decreases as the Ca^{2+} concentration increases (with an apparent K_D of 64.7 ± 18.8 μM; Figures 4C and 4D). Moreover, NTD did not bind to a proteoliposome incorporated with a bacterial homolog of the tryptophan-rich sensory protein (TSPO) expressed in the mitochondrial outer membrane, in either presence or absence of Ca^{2+} (Figure S5). This further supports the specific interaction between NTD and TMD of SCaMC1.

We then examined NTD-TMD interaction using NMR with the attempt to map interactions between NTD and detergent-solubilized TMD. However, as indicated by our NMR spectra (Figure S4B), the NTD is incompatible with the detergents we tested, i.e., it unfolded and/or aggregated at as low as 2 critical micelle concentration of commonly used detergents including n-dodecyl β-D-maltoside, n-dodecyl-N,N-dimethylamine-N-oxide, and DPC. On the other hand, when titrating with empty POPC/POPG/cardiolipin liposome, the NTD spectrum was unaffected (Figures S4C and S4D), indicating that the protein does not interact with lipid bilayers. Thus, we investigated interaction between NTD and TMD proteoliposome by NMR. In the absence of Ca^{2+}, titrating NTD with TMD proteoliposome caused drastic broadening of the NMR spectrum. Most resonances disappeared except those of flexible regions (Figure 4E). This observation is expected. Due to the slow tumbling of the large proteoliposomes, NMR resonances of the regions of NTD that directly interact with the TMD are expected to severely broaden

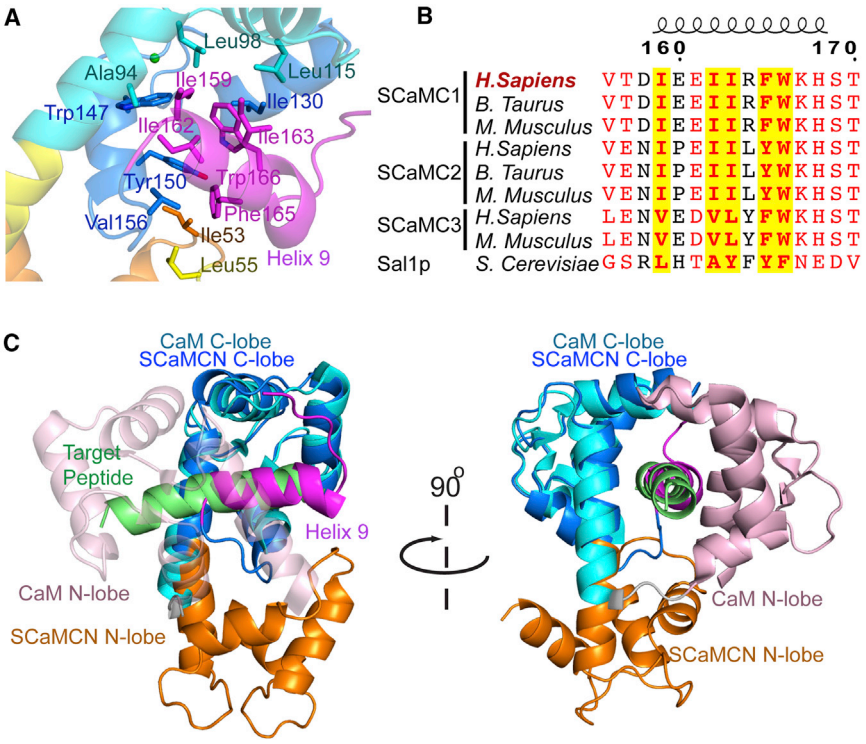

Figure 2. H9 Appears to Be an Intramolecular Target Peptide for the SCaMC EF Hands

(A) Detailed view of H9 interacting with EF hands III and IV, showing the residues involved in the interaction. The color scheme used is the same as in Figure 1.

(B) Sequence alignment of H9 from SCaMC paralogs and homologs. Residues with more than 70% conservation are colored in red. The five hydrophobic residues involved in binding to the EF hands are highlighted in yellow. A more complete alignment is shown in Figure S3.

(C) Structure alignment between Ca^{2+}-NTD and CaM-peptide complex. The N- and C-lobes of NTD are colored in orange and blue, respectively, whereas the CaM N- and C-lobes are in pink and cyan, respectively. The SCaMC-1 H9 (magenta) aligns well with the target peptide of CaM (green) in the CaM-peptide complex.

and vanish, whereas those of disordered loops should still have sufficiently long T_2 to be observed. More specifically, the remaining resonances correspond to highly dynamic regions including residues 53–72 and residues 172–193 (which connect NTD and TMD in the full-length SCaMC-1), whereas resonances for the structured regions disappeared. The results indicate that apo NTD could directly interact with certain regions of the TMD. In contrast, in the presence of Ca^{2+}, NTD spectrum did not show any noticeable broadening upon the addition of TMD proteoliposomes (Figure 4F), indicating that the Ca^{2+}-bound structure of NTD does not support specific interaction with the TMD.

DISCUSSION

The structural and functional data we have presented show that SCaMC NTD can undergo large conformational changes triggered by Ca^{2+} binding and that this conformational switch may play a role in Ca^{2+}-dependent regulation of the ATP-Mg transport activity of TMD. The crystal structure of the Ca^{2+}-bound state of NTD shows a compact and rigid structure that appears to preclude the EF hands from interacting with any target peptides. The compactness of the NTD is in striking difference with CaM in its Ca^{2+}-bound form. For CaM, in the presence of Ca^{2+}, the central linker adopts an extended form that separates N- and C-lobes (Chou et al., 2001). In the Ca^{2+}-bound SCaMC-1 NTD, however, the corresponding central linker essentially does not exist, thus resulting in the formation of a continuous central helix that constitutively places the N- and C-lobes in proximity. In this conformation, the N-lobe EF hands are preoccupied with interaction with the C-lobe EF hand, whereas the otherwise exposed hydrophobic clamps of EF hands III and IV are sequestered by H9 (Figure 1A). Therefore, the Ca^{2+}-bound NTD does not appear to be in a conformation capable of interacting with any peptide substrates, and this is consistent with our NMR titration and SPR data that, in the presence of Ca^{2+}, NTD has very weak, if any, interactions with the liposome-incorporated TMD. The self-sequestered conformation above resembles the autoregulation mechanism of the STIMs, in which two EF hands of STIMs bind to an appended helix in the presence of Ca^{2+} to form a compact conformation and maintain its monomeric status (the inactive state; Stathopulos et al., 2008). Depletion of Ca^{2+} from STIMs leads to EF hands' conformational change and subsequent oligomerization (the active state; Zheng et al., 2011).

In the absence of Ca^{2+}, the NTD has drastically different structural properties than the Ca^{2+}-bound state, as indicated by the different NMR spectra and relaxation rates. Whereas the NMR relaxation rates for the Ca^{2+}-bound state are uniform throughout most of the protein, they became very heterogeneous in the apo state (Figure 3). The relaxation rates and heteronuclear NOE data indicated that residues 50–78 become essentially unfolded in the apo state. Moreover, the H9 has different relaxation properties as the EF hand III and IV to which it binds in the Ca^{2+}-bound state, indicating that in the apo state this helix no longer interacts with the EF hands. We did not observe resonances for residues 139–155, probably due to solvent exchange and/or exchange broadening. Since the interactions between residues 51–59 and 152–159 are the primary forces holding N- and C-lobes together, the unfolding of the above regions is expected to expose a large surface to bind TMD (Figure 3G). Indeed, as demonstrated by our SPR measurements, the apo state of NTD could specifically bind to TMD reconstituted in liposomes (K_D of ~250 μM), but the Ca^{2+}-bound form did not. Furthermore, the dependence of interaction between NTD and TMD on Ca^{2+} (apparent K_D of ~65 μM) is similar to the half-maximal activation Ca^{2+} concentration determined by Ca^{2+}-activated ATP transport in mitochondria of COS-7 cell line (12 μM; Traba et al., 2012) and in *Saccharomyces cerevisiae* (~20 μM; Cavero et al., 2005; Traba et al., 2008). Although we were not able to determine a

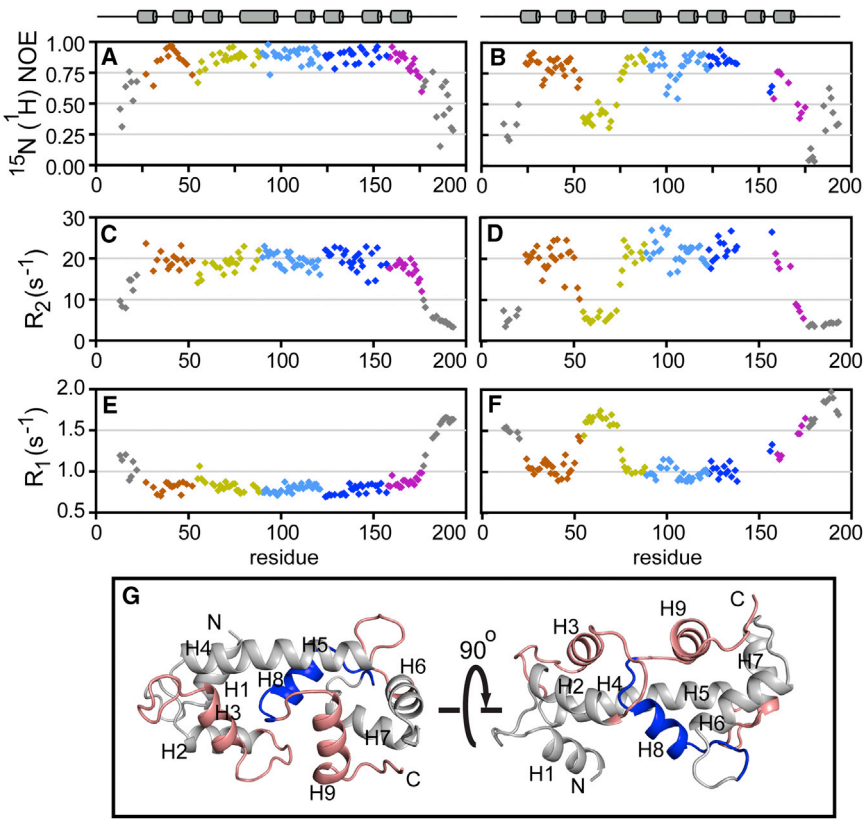

Figure 3. The apo NTD Is More Dynamic and Less Structured than Ca^{2+}-Bound NTD

(A–F) Residue-specific heteronuclear $^{15}N(^{1}H)$ NOE, R_2, and R_1 values of the Ca^{2+}-bound NTD, measured at 30°C and ^{1}H frequency of 750 MHz (A, C, and E), and the corresponding NOE and relaxation rates for the apo NTD (B, D, and F). Secondary structure elements of the Ca^{2+}-bound NTD are indicated above the plots. The color scheme used here is the same as in Figure 1A. See also Figure S1.

(G) The flexible regions ($^{15}N(^{1}H)$ NOE < 0.75) found in the apo NTD (salmon) are mapped onto the structure of the Ca^{2+}-bound NTD, for showing regions of the Ca^{2+}-bound NTD that become largely disordered in the absence of Ca^{2+}. The unassigned residues (139–155) in the apo state are colored in blue.

conformation representing the dynamic apo NTD, the NMR dynamics data clearly indicate that the apo state is a much less compact, less structured, and more dynamic state.

Based on the above results, we propose that, in the absence of Ca^{2+}, NTD acts as a cap that physically blocks substrate transport (Figure 5). Although it is unusual that the apo, not the Ca^{2+}-bound, EF hands represent the state responsible for target recognition, there are earlier precedents of apo CaM capable of binding target peptides of myosine (Houdusse et al., 2006) and voltage-gated sodium channel (Chagot and Chazin, 2011; Wang et al., 2012) as part of its regulatory mechanism. The Ca^{2+}-dependent capping/uncapping mechanism is in good agreement with previous functional observations. First, Ca^{2+} stimulates ATP import in the mitochondria of rat liver (Nosek et al., 1990), human osteosarcoma cell line 143B (Traba et al., 2012), and *S. cerevisiae* (Chen, 2004). Second, Ca^{2+} only alters ATP-Mg translocation rates, but not the binding affinity for ATP-Mg (Dransfield and Aprille, 1993; Tewari et al., 2012; Traba et al., 2008). Third, loss of the entire NTD leads to a constitutively active variant SCaMC-3L (Traba et al., 2009a), whereas Sal1p mutants with impaired Ca^{2+} binding displayed a defective ATP transport, possibly due to the inability to convert the apo to Ca^{2+}-bound form (Chen, 2004). It is interesting from an evolutionary perspective that none of the SCaMC variants show any amino acid substitutions for the EF hands (Satrústegui et al., 2007), as these variants would otherwise result in permanently inactivated SCaMC and thus impaired growth. It is also interesting that aspartate/glutamate carrier (AGC), another one of the two carriers that possess N-terminal CaM-like domain, is also activated by Ca^{2+} (Palmieri et al., 2001), and this carrier may use a similar capping/uncapping mechanism to regulate solute transport.

Ca^{2+} is one of the most important secondary signaling messengers, involved in a wide range of physiological regulations, but adoption of a CaM-like Ca^{2+}-sensing domain by a membrane transporter to directly regulate its transport activity is unusual. The voltage-gated Na^{+} channels (Shah et al., 2006) and the voltage-gated Ca^{2+} channels (Johny et al., 2013) are among the few ion channels that use covalently tethered EF-hand motifs for mediating Ca^{2+} regulation of channel activity, but such regulation also requires intermolecular interaction with CaM (Chagot and Chazin, 2011; Johny et al., 2013; Van Petegem et al., 2005). To the best of our knowledge, SCaMC and AGC are the only two transporters known thus far that use a covalently linked domain to regulate transport activities in a Ca^{2+}-dependent manner (del Arco and Satrústegui, 2004; Palmieri et al., 2001). This unusual structural feature entitles SCaMC an important role in the regulation of energy metabolism. Since SCaMC NTD is in the intermembrane space, it senses cytosolic Ca^{2+} concentration fluctuation and can transmit Ca^{2+} signal without the need to transport Ca^{2+} into the matrix. This provides an indirect Ca^{2+} signaling pathway in additional to those that require the import of Ca^{2+} into the matrix, e.g., the mitochondrial Ca^{2+} uniporter mediated pathway (Baughman et al., 2011). In accordance with the role of Ca^{2+} as signal for increased energy requirements, Ca^{2+} binding to NTD releases autoinhibition of SCaMC, which leads to increased matrix adenine nucleotide content and subsequently stimulates oxidative phosphorylation (Amigo et al., 2013). Knockout of SCaMC gene in mice resulted in lower cellular ATP levels, reduced physical endurance, and metabolic efficiency (Anunciado-Koza et al., 2011).

In conclusion, we have shown that the extramembrane NTD of SCaMC-1 undergoes a large structural change triggered by Ca^{2+} binding and that this conformational switch directly impacts its ability to interact with the TMD as a part of Ca^{2+} regulation of

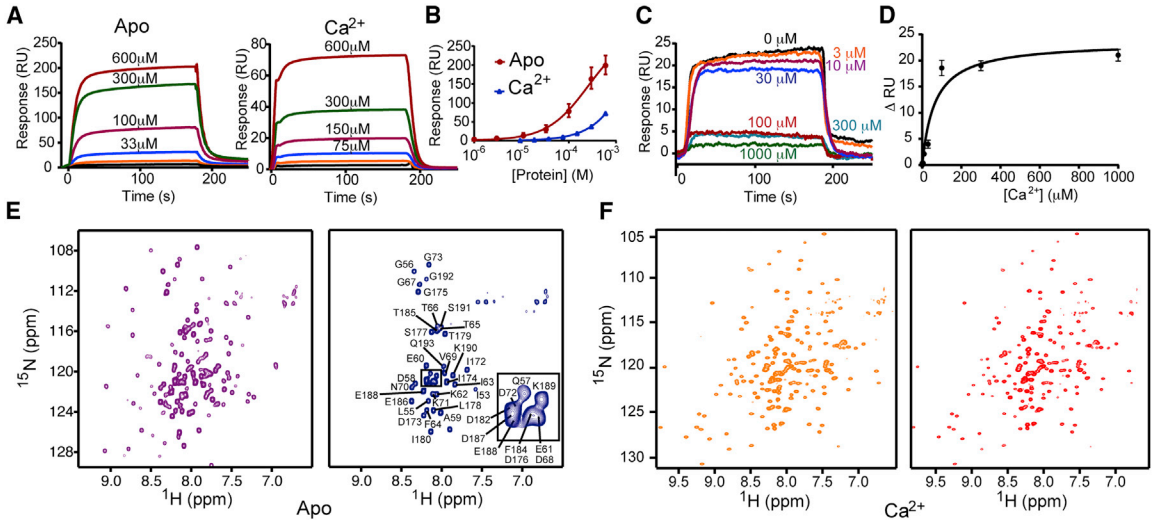

Figure 4. The apo NTD, but Not the Ca^{2+}-Bound NTD, Binds Specifically to TMD

(A) SPR sensorgrams of the binding of NTD to immobilized TMD proteoliposomes at different NTD concentrations in the absence of Ca^{2+} (left) and in the presence of 5 mM Ca^{2+} (right).

(B) Binding isotherms derived from data in (A) determined K_D of 250 ± 50 μM for the apo NTD and 5,600 ± 1,000 μM for the Ca^{2+}-bound NTD. In this analysis, equilibrium signals at various NTD concentrations were plotted and fit with a single binding isotherm to determine K_D. The K_D values presented are mean ± SD, calculated from three independent measurements.

(C) SPR sensorgrams of the binding of 33 μM NTD, which does not contain EDTA, to the immobilized TMD proteoliposomes in the presence of 0, 3, 10, 30, 100, 300, and 1,000 μM of Ca^{2+}.

(D) Binding isotherms derived from data in (C) determined apparent K_D of 64.7 ± 18.8 μM for Ca^{2+}. In this analysis, the RU at 0 μM Ca^{2+} was used as a reference point, and the change in RU (ΔRU) as compared to 0 μM Ca^{2+} for the rest of the data points was plotted and fit with a single binding isotherm to determine apparent K_D. Error bars represent SD of the two measurements. The K_D values presented are mean ± SD, calculated from two independent measurements. See also Figure S5.

(E) The ^1H-^{15}N TROSY-HSQC spectra of 0.1 mM apo NTD in the presence of empty liposomes (left) or 0.1 mM TMD incorporated proteoliposomes (right), both containing 20 mM total lipid. The majority of the peaks disappeared with the exception of the dynamic regions, residues 53–72 and 172–193.

(F) The same spectra as in (C) recorded for Ca^{2+}-bound NTD, showing essentially no change in the presence of the TMD. See also Figure S4.

ATP-Mg transport. In the absence of Ca^{2+}, NTD is partially unfolded in solution and binds specifically to TMD, whereas in the presence of Ca^{2+} it adopts a rigid and compact structure that largely abrogates TMD binding. An unexpected feature of the Ca^{2+}-bound state was a C-terminal helix that appeared to serve as an endogenous inhibitory domain that sequesters the EF hands from target interaction. Our structural and biochemical data, together with earlier functional results of Ca^{2+}-induced activation of ATP-Mg transport of SCaMC, suggest a capping mechanism of SCaMC by which the apo NTD caps the TMD channel from the intermembrane space of mitochondria and blocks substrate transport, whereas Ca^{2+} binding converts NTD to a self-sequestered form that uncaps the channel. Although this model remains to be tested by further structural investigations of the NTD-TMD complex, it represents a significant step toward the structural basis of Ca^{2+} regulation of ATP-Mg transport by the SCaMC transporters.

EXPERIMENTAL PROCEDURES

X-Ray Crystallography and NMR Spectroscopy

Human SCaMC-1 NTD (residues 1–193) was expressed in BL21 (DE3) cells and purified with cobalt resin and a Superdex S75-size exclusion column. The purified NTD fraction was in the Ca^{2+}-bound form. The apo form of NTD was obtained by extensive dialysis against buffer containing EDTA. The Ca^{2+}-bound NTD was crystallized in two forms with space groups $P6_222$ and $P3_121$. Attempts to crystallize NTD in the absence of Ca^{2+} were unsuccessful. The ^1H-^{15}N RDCs of the Ca^{2+}-bound NTDs were measured using ^{15}N-labeled protein weakly aligned in filamentous phage Pf1. Relaxation rates ^{15}N R_1 and R_2 and $^{15}N(^1H)$ NOE for apo and Ca^{2+}-bound NTDs were measured using the standard pulse schemes described previously (Kay et al., 1989). Details of data collection and analysis are provided in Supplemental Experimental Procedures.

Proteoliposome Binding Measurements

TMD (residues 185–477) was expressed in BL21 (DE3) cells and purified using a protocol similar to that previously reported (Berardi et al., 2011). TMD proteoliposome is prepared as described in Supplemental Experimental Procedures. The liposome is composed of POPC, POPG, and cardiolipin at 4:1:0.1 molar ratio. The final proteoliposome solution contained 40 mM total lipid and 0.2 mM TMD for NMR experiments or 0.5 mM total lipid and 2.5 μM TMD for SPR experiments. Empty liposomes were prepared in the same way without the protein. For NMR measurements of NTD-TMD interaction, 0.2 mM ^{15}N-labeled NTD in the NMR buffer was mixed with equal volume of either TMD proteoliposome or empty liposome solution above.

SPR experiments were performed using a protocol similar to that described previously (Hodnik and Anderluh, 2010; Stahelin, 2013). TMD proteoliposomes or empty liposomes were immobilized in active flow cell or control flow cell of L1 sensor chip, respectively. To measure binding, apo or Ca^{2+}-bound NTDs were injected at increasing concentrations and the responses in signal (response units [RU]) were recorded. Sensorgrams were corrected for changes in the refractive index of the buffer and nonspecific binding by subtracting the response of the control flow cell with immobilized empty liposomes. Equilibrium signal (R_{eq}) at a given NTD concentration (C) was plotted and fit to the equation $R_{eq} = R_{max}/(1 + K_D/C)$ to determine the equilibrium binding constant (K_D). R_{max} is the binding signal at saturation. More details are provided in Supplemental Experimental Procedures.

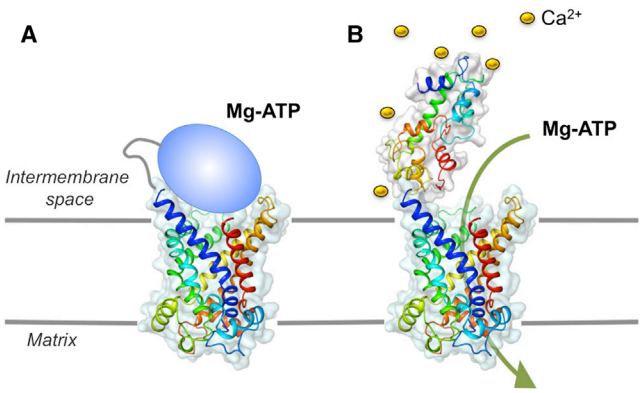

Figure 5. A Proposed Model for Ca^{2+}-Regulated ATP-Mg/P_i Transport by SCaMC

(A) In the absence of Ca^{2+}, the NTD has a dynamic and loose conformation; it can specifically interact with and probably undergo conformational change and "cap" the intermembrane space side of the TMD. The apo form NTD is represented by the ellipsoid.

(B) In the presence of Ca^{2+}, the NTD is in a compact and self-sequestered form that no longer interacts with the TMD. The "uncapping" allows solutes to be transported. The TMD structure was modeled after the crystal structure of the inhibited state of the ADP/ATP carrier (PDB ID code 1OKC).

ACCESSION NUMBERS

Coordinates of Ca^{2+}-bound SCaMC-1 NTD have been deposited in the RCSB Protein Data Bank under the accession code 4N5X.

SUPPLEMENTAL INFORMATION

Supplemental Information includes Supplemental Experimental Procedures and five figures and can be found with this article online at http://dx.doi.org/10.1016/j.str.2013.10.018.

ACKNOWLEDGMENTS

We thank members of the Chou Lab for technical assistance and insightful discussions, Dr. Kirill Oxenoid for TSPO protein, Dr. Longfei Wang for help with SPR experiments, and Dr. Yu Chen (Harvard Medical School) for X-ray data collection. This work is based upon research conducted at the Advanced Photon Source (Northeastern Collaborative Access Team beamlines). S.B. is a recipient of an Erwin Schrödinger postdoctoral fellowship of the Austrian Science Fund (FWF, J3251). This work was supported by NIH grant GM094608 (to J.J.C.).

Received: August 27, 2013
Revised: October 11, 2013
Accepted: October 29, 2013
Published: December 12, 2013

REFERENCES

Amigo, I., Traba, J., Satrústegui, J., and del Arco, A. (2012). SCaMC-1Like a member of the mitochondrial carrier (MC) family preferentially expressed in testis and localized in mitochondria and chromatoid body. PLoS ONE *7*, e40470.

Amigo, I., Traba, J., González-Barroso, M.M., Rueda, C.B., Fernández, M., Rial, E., Sánchez, A., Satrústegui, J., and Del Arco, A. (2013). Glucagon regulation of oxidative phosphorylation requires an increase in matrix adenine nucleotide content through Ca2+ activation of the mitochondrial ATP-Mg/Pi carrier SCaMC-3. J. Biol. Chem. *288*, 7791–7802.

Anunciado-Koza, R.P., Zhang, J., Ukropec, J., Bajpeyi, S., Koza, R.A., Rogers, R.C., Cefalu, W.T., Mynatt, R.L., and Kozak, L.P. (2011). Inactivation of the mitochondrial carrier SLC25A25 (ATP-Mg2+/Pi transporter) reduces physical endurance and metabolic efficiency in mice. J. Biol. Chem. *286*, 11659–11671.

Barbato, G., Ikura, M., Kay, L.E., Pastor, R.W., and Bax, A. (1992). Backbone dynamics of calmodulin studied by 15N relaxation using inverse detected two-dimensional NMR spectroscopy: the central helix is flexible. Biochemistry *31*, 5269–5278.

Bassi, M.T., Manzoni, M., Bresciani, R., Pizzo, M.T., Della Monica, A., Barlati, S., Monti, E., and Borsani, G. (2005). Cellular expression and alternative splicing of SLC25A23, a member of the mitochondrial Ca2+-dependent solute carrier gene family. Gene *345*, 173–182.

Baughman, J.M., Perocchi, F., Girgis, H.S., Plovanich, M., Belcher-Timme, C.A., Sancak, Y., Bao, X.R., Strittmatter, L., Goldberger, O., Bogorad, R.L., et al. (2011). Integrative genomics identifies MCU as an essential component of the mitochondrial calcium uniporter. Nature *476*, 341–345.

Berardi, M.J., Shih, W.M., Harrison, S.C., and Chou, J.J. (2011). Mitochondrial uncoupling protein 2 structure determined by NMR molecular fragment searching. Nature *476*, 109–113.

Cavero, S., Traba, J., Del Arco, A., and Satrústegui, J. (2005). The calcium-dependent ATP-Mg/Pi mitochondrial carrier is a target of glucose-induced calcium signalling in Saccharomyces cerevisiae. Biochem. J. *392*, 537–544.

Chagot, B., and Chazin, W.J. (2011). Solution NMR structure of Apo-calmodulin in complex with the IQ motif of human cardiac sodium channel NaV1.5. J. Mol. Biol. *406*, 106–119.

Chen, X.J. (2004). Sal1p, a calcium-dependent carrier protein that suppresses an essential cellular function associated with the Aac2 isoform of ADP/ATP translocase in Saccharomyces cerevisiae. Genetics *167*, 607–617.

Chen, Y.W., Chou, H.C., Lyu, P.C., Yin, H.S., Huang, F.L., Chang, W.S., Fan, C.Y., Tu, I.F., Lai, T.C., Lin, S.T., et al. (2011). Mitochondrial proteomics analysis of tumorigenic and metastatic breast cancer markers. Funct. Integr. Genomics *11*, 225–239.

Chou, J.J., Li, S., Klee, C.B., and Bax, A. (2001). Solution structure of Ca(2+)-calmodulin reveals flexible hand-like properties of its domains. Nat. Struct. Biol. *8*, 990–997.

Clapham, D.E. (2007). Calcium signaling. Cell *131*, 1047–1058.

Dehez, F., Pebay-Peyroula, E., and Chipot, C. (2008). Binding of ADP in the mitochondrial ADP/ATP carrier is driven by an electrostatic funnel. J. Am. Chem. Soc. *130*, 12725–12733.

del Arco, A., and Satrústegui, J. (2004). Identification of a novel human subfamily of mitochondrial carriers with calcium-binding domains. J. Biol. Chem. *279*, 24701–24713.

Doublié, S. (2007). Production of selenomethionyl proteins in prokaryotic and eukaryotic expression systems. Methods Mol. Biol. *363*, 91–108.

Dransfield, D.T., and Aprille, J.R. (1993). Regulation of the mitochondrial ATP-Mg/Pi carrier in isolated hepatocytes. Am. J. Physiol. *264*, C663–C670.

Fiermonte, G., De Leonardis, F., Todisco, S., Palmieri, L., Lasorsa, F.M., and Palmieri, F. (2004). Identification of the mitochondrial ATP-Mg/Pi transporter. Bacterial expression, reconstitution, functional characterization, and tissue distribution. J. Biol. Chem. *279*, 30722–30730.

Gifford, J.L., Walsh, M.P., and Vogel, H.J. (2007). Structures and metal-ion-binding properties of the Ca2+-binding helix-loop-helix EF-hand motifs. Biochem. J. *405*, 199–221.

Hagen, T., Joyal, J.L., Henke, W., and Aprille, J.R. (1993). Net adenine nucleotide transport in rat kidney mitochondria. Arch. Biochem. Biophys. *303*, 195–207.

Hodnik, V., and Anderluh, G. (2010). Capture of intact liposomes on biacore sensor chips for protein-membrane interaction studies. Methods Mol. Biol. *627*, 201–211.

Hoeflich, K.P., and Ikura, M. (2002). Calmodulin in action: diversity in target recognition and activation mechanisms. Cell *108*, 739–742.

Houdusse, A., Gaucher, J.F., Krementsova, E., Mui, S., Trybus, K.M., and Cohen, C. (2006). Crystal structure of apo-calmodulin bound to the first two

IQ motifs of myosin V reveals essential recognition features. Proc. Natl. Acad. Sci. USA *103*, 19326–19331.

Ikura, M., Clore, G.M., Gronenborn, A.M., Zhu, G., Klee, C.B., and Bax, A. (1992). Solution structure of a calmodulin-target peptide complex by multidimensional NMR. Science *256*, 632–638.

Johny, M.B., Yang, P.S., Bazzazi, H., and Yue, D.T. (2013). Dynamic switching of calmodulin interactions underlies Ca(2+) regulation of CaV1.3 channels. Nat. Commun. *4*, 1717.

Kay, L.E., Torchia, D.A., and Bax, A. (1989). Backbone dynamics of proteins as studied by 15N inverse detected heteronuclear NMR spectroscopy: application to staphylococcal nuclease. Biochemistry *28*, 8972–8979.

Klingenberg, M. (2009). Cardiolipin and mitochondrial carriers. Biochim. Biophys. Acta *1788*, 2048–2058.

Kuboniwa, H., Tjandra, N., Grzesiek, S., Ren, H., Klee, C.B., and Bax, A. (1995). Solution structure of calcium-free calmodulin. Nat. Struct. Biol. *2*, 768–776.

Kucejova, B., Li, L., Wang, X., Giannattasio, S., and Chen, X.J. (2008). Pleiotropic effects of the yeast Sal1 and Aac2 carriers on mitochondrial function via an activity distinct from adenine nucleotide transport. Mol. Genet. Genomics *280*, 25–39.

Kunji, E.R., and Harding, M. (2003). Projection structure of the atractyloside-inhibited mitochondrial ADP/ATP carrier of Saccharomyces cerevisiae. J. Biol. Chem. *278*, 36985–36988.

Kunji, E.R., and Robinson, A.J. (2010). Coupling of proton and substrate translocation in the transport cycle of mitochondrial carriers. Curr. Opin. Struct. Biol. *20*, 440–447.

Llorente-Folch, I., Rueda, C.B., Amigo, I., del Arco, A., Saheki, T., Pardo, B., and Satrústegui, J. (2013). Calcium-regulation of mitochondrial respiration maintains ATP homeostasis and requires ARALAR/AGC1-malate aspartate shuttle in intact cortical neurons. J. Neurosci. *33*, 13957–13971.

Mashima, H., Ueda, N., Ohno, H., Suzuki, J., Ohnishi, H., Yasuda, H., Tsuchida, T., Kanamaru, C., Makita, N., Iiri, T., et al. (2003). A novel mitochondrial Ca2+-dependent solute carrier in the liver identified by mRNA differential display. J. Biol. Chem. *278*, 9520–9527.

Meador, W.E., Means, A.R., and Quiocho, F.A. (1992). Target enzyme recognition by calmodulin: 2.4 A structure of a calmodulin-peptide complex. Science *257*, 1251–1255.

Nosek, M.T., Dransfield, D.T., and Aprille, J.R. (1990). Calcium stimulates ATP-Mg/Pi carrier activity in rat liver mitochondria. J. Biol. Chem. *265*, 8444–8450.

Palmieri, L., Pardo, B., Lasorsa, F.M., del Arco, A., Kobayashi, K., Iijima, M., Runswick, M.J., Walker, J.E., Saheki, T., Satrústegui, J., and Palmieri, F. (2001). Citrin and aralar1 are Ca(2+)-stimulated aspartate/glutamate transporters in mitochondria. EMBO J. *20*, 5060–5069.

Palmieri, F., Agrimi, G., Blanco, E., Castegna, A., Di Noia, M.A., Iacobazzi, V., Lasorsa, F.M., Marobbio, C.M., Palmieri, L., Scarcia, P., et al. (2006). Identification of mitochondrial carriers in Saccharomyces cerevisiae by transport assay of reconstituted recombinant proteins. Biochim. Biophys. Acta *1757*, 1249–1262.

Palmieri, F., Pierri, C.L., De Grassi, A., Nunes-Nesi, A., and Fernie, A.R. (2011). Evolution, structure and function of mitochondrial carriers: a review with new insights. Plant J. *66*, 161–181.

Pebay-Peyroula, E., Dahout-Gonzalez, C., Kahn, R., Trézéguet, V., Lauquin, G.J., and Brandolin, G. (2003). Structure of mitochondrial ADP/ATP carrier in complex with carboxyatractyloside. Nature *426*, 39–44.

Satrústegui, J., Pardo, B., and Del Arco, A. (2007). Mitochondrial transporters as novel targets for intracellular calcium signaling. Physiol. Rev. *87*, 29–67.

Shah, V.N., Wingo, T.L., Weiss, K.L., Williams, C.K., Balser, J.R., and Chazin, W.J. (2006). Calcium-dependent regulation of the voltage-gated sodium channel hH1: intrinsic and extrinsic sensors use a common molecular switch. Proc. Natl. Acad. Sci. USA *103*, 3592–3597.

Stahelin, R.V. (2013). Surface plasmon resonance: a useful technique for cell biologists to characterize biomolecular interactions. Mol. Biol. Cell *24*, 883–886.

Stathopulos, P.B., Zheng, L., Li, G.Y., Plevin, M.J., and Ikura, M. (2008). Structural and mechanistic insights into STIM1-mediated initiation of store-operated calcium entry. Cell *135*, 110–122.

Taylor, D.A., Sack, J.S., Maune, J.F., Beckingham, K., and Quiocho, F.A. (1991). Structure of a recombinant calmodulin from Drosophila melanogaster refined at 2.2-A resolution. J. Biol. Chem. *266*, 21375–21380.

Tewari, S.G., Dash, R.K., Beard, D.A., and Bazil, J.N. (2012). A biophysical model of the mitochondrial ATP-Mg/P(i) carrier. Biophys. J. *103*, 1616–1625.

Tjandra, N., Kuboniwa, H., Ren, H., and Bax, A. (1995). Rotational dynamics of calcium-free calmodulin studied by 15N-NMR relaxation measurements. Eur. J. Biochem. *230*, 1014–1024.

Traba, J., Froschauer, E.M., Wiesenberger, G., Satrústegui, J., and Del Arco, A. (2008). Yeast mitochondria import ATP through the calcium-dependent ATP-Mg/Pi carrier Sal1p, and are ATP consumers during aerobic growth in glucose. Mol. Microbiol. *69*, 570–585.

Traba, J., Satrústegui, J., and del Arco, A. (2009a). Characterization of SCaMC-3-like/slc25a41, a novel calcium-independent mitochondrial ATP-Mg/Pi carrier. Biochem. J. *418*, 125–133.

Traba, J., Satrústegui, J., and del Arco, A. (2009b). Transport of adenine nucleotides in the mitochondria of Saccharomyces cerevisiae: interactions between the ADP/ATP carriers and the ATP-Mg/Pi carrier. Mitochondrion *9*, 79–85.

Traba, J., Satrústegui, J., and del Arco, A. (2011). Adenine nucleotide transporters in organelles: novel genes and functions. Cell. Mol. Life Sci. *68*, 1183–1206.

Traba, J., Del Arco, A., Duchen, M.R., Szabadkai, G., and Satrústegui, J. (2012). SCaMC-1 promotes cancer cell survival by desensitizing mitochondrial permeability transition via ATP/ADP-mediated matrix Ca(2+) buffering. Cell Death Differ. *19*, 650–660.

Van Petegem, F., Chatelain, F.C., and Minor, D.L., Jr. (2005). Insights into voltage-gated calcium channel regulation from the structure of the CaV1.2 IQ domain-Ca2+/calmodulin complex. Nat. Struct. Mol. Biol. *12*, 1108–1115.

Walker, J.E., and Runswick, M.J. (1993). The mitochondrial transport protein superfamily. J. Bioenerg. Biomembr. *25*, 435–446.

Wang, C., Chung, B.C., Yan, H., Lee, S.Y., and Pitt, G.S. (2012). Crystal structure of the ternary complex of a NaV C-terminal domain, a fibroblast growth factor homologous factor, and calmodulin. Structure *20*, 1167–1176.

Wingo, T.L., Shah, V.N., Anderson, M.E., Lybrand, T.P., Chazin, W.J., and Balser, J.R. (2004). An EF-hand in the sodium channel couples intracellular calcium to cardiac excitability. Nat. Struct. Mol. Biol. *11*, 219–225.

Yang, Q., Coseno, M., Gilmartin, G.M., and Doublié, S. (2011). Crystal structure of a human cleavage factor CFI(m)25/CFI(m)68/RNA complex provides an insight into poly(A) site recognition and RNA looping. Structure *19*, 368–377.

Zheng, L., Stathopulos, P.B., Schindl, R., Li, G.Y., Romanin, C., and Ikura, M. (2011). Auto-inhibitory role of the EF-SAM domain of STIM proteins in store-operated calcium entry. Proc. Natl. Acad. Sci. USA *108*, 1337–1342.

Supplemental Information

A self-sequestered calmodulin-like Ca^{2+} sensor of mitochondrial SCaMC carrier and its implication to Ca^{2+}-dependent ATP-Mg/Pi transport

Qin Yang, Sven Brueschweiler and James J. Chou*

Supplemental Figures

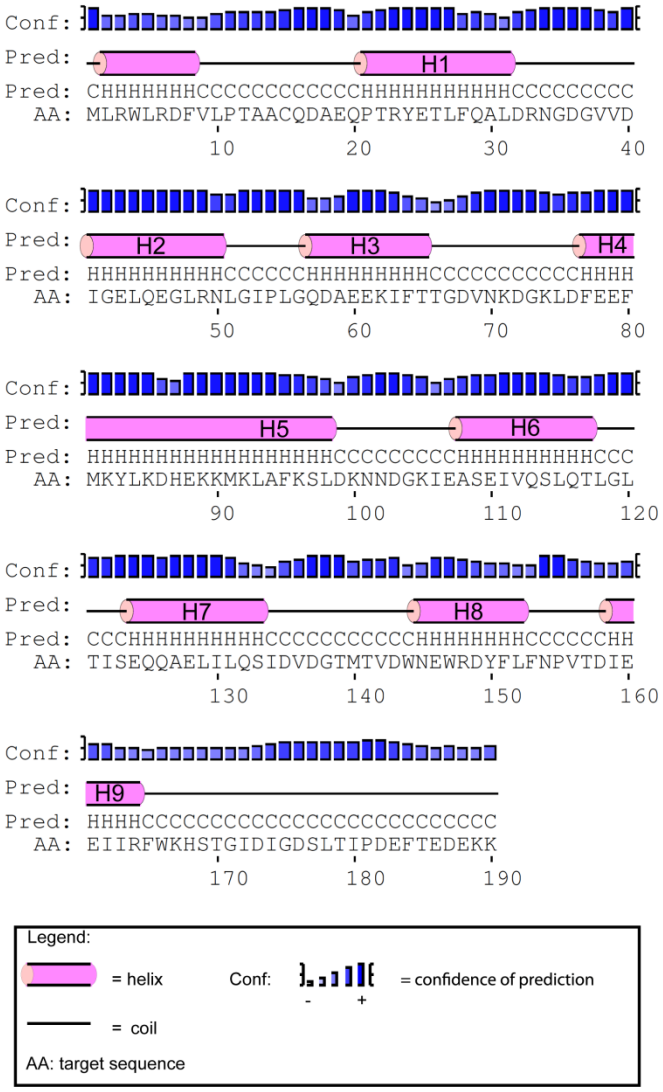

Figure S1. Secondary structure prediction of human SCaMC-1 NTD

Secondary structure prediction of human SCaMC-1 NTD was performed using the PSIPRED secondary structure prediction method (Jones, 1999). The predicted helices are shown as pink tubes and numbered as in Figure 1B. Otherwise, the lines represent predicted coil regions. Residue-specific confidences of prediction are represented by blue bars. Although residues 2-8 were predicted to form helix, we did not observe either crystallographic densities or NMR resonances for these residues.

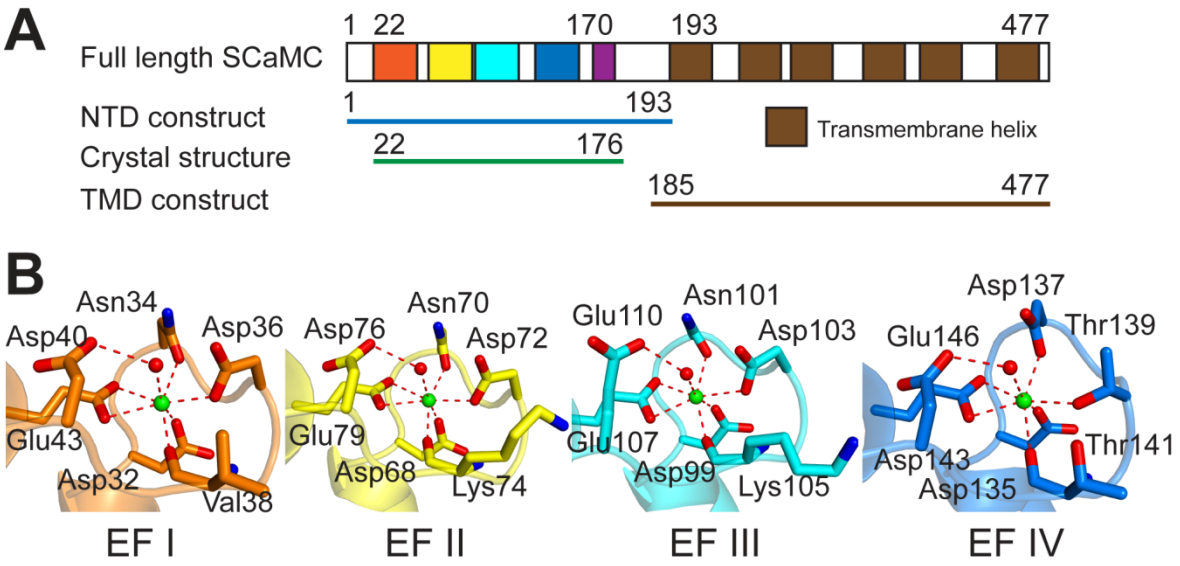

Figure S2. Domain organization and Ca^{2+} coordination of the human SCaMC-1

(A) Full-length SCaMC-1 consists of the CaM-like domain (residues 1-170), the substrate-transporting domain (residues 193-477), and the intervening loop (residues 171-192). EF-hands are colored in orange, yellow, cyan, and blue. The extra helix (H9) after the CaM-like domain is colored in magenta. Transmembrane helices in the substrate-transporting domain are colored in brown. The NTD construct used for structure determination consists of residues 1-193, but electron density was observed only for residues 22-173.The TMD construct consisted of residue 185-477 were used for studying TMD-NTD interactions.

(**B**) Close-up views of the Ca^{2+}-binding loops of the EF hands, showing residues participating in Ca^{2+} coordination. Water molecules are shown as red spheres. The red, dashed lines represent hydrogen bonds.

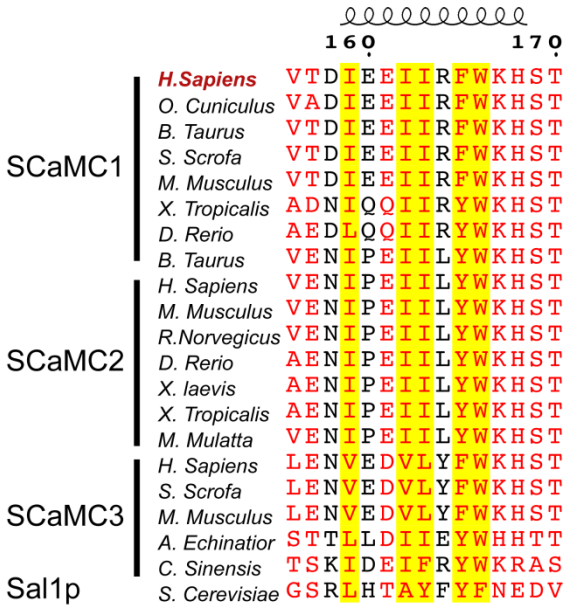

Figure S3. Sequence alignment of the internal target peptide H9 of SCaMC

Sequences encompassing the H9 helix from 21 SCaMC paralogs and homologs (from the UniProtKB database) are aligned using program ClustalW2 (Goujon et al., 2010). SCaMC is named as Sal1p in *Saccharomyces cerevisiae*. Residues with more than 70% conservation are colored in red. The five hydrophobic residues involved in binding to the EF hands are highlighted in yellow. The figure was generated using program ESPript (Gouet et al., 1999).

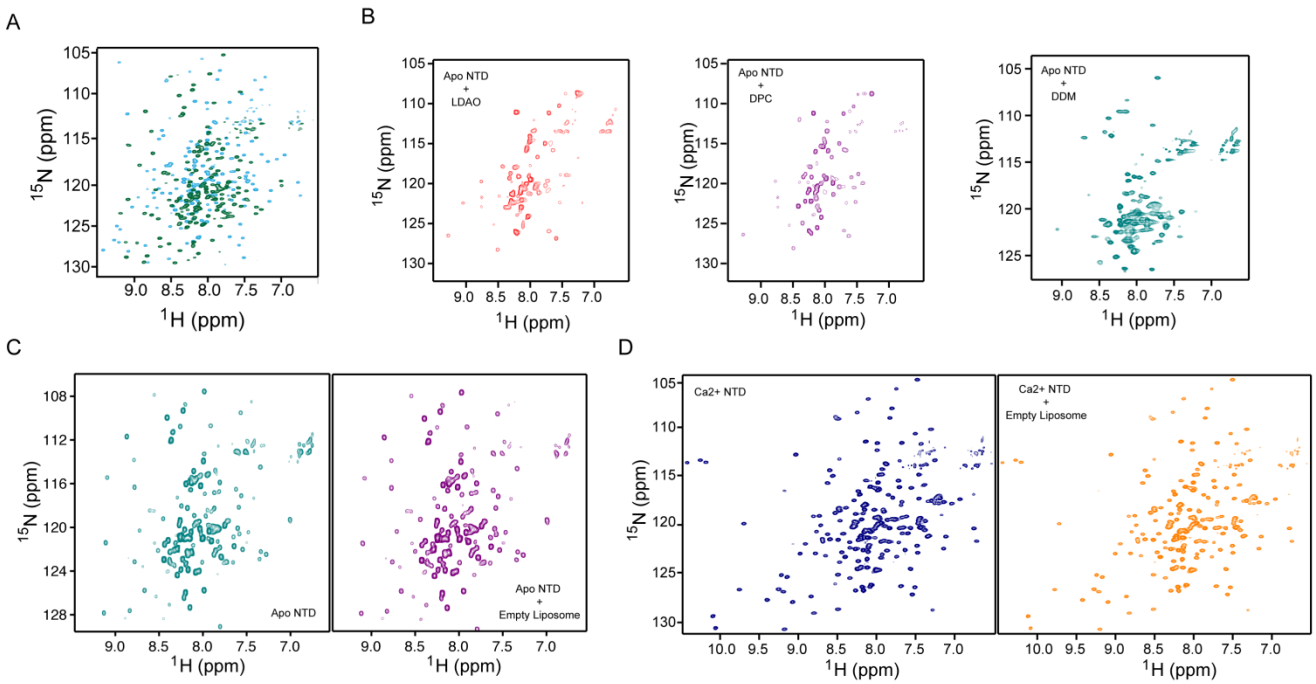

Figure S4. Ca^{2+}-binding triggers conformational change in NTD, and NTD is compatible with liposomes but not with detergents

(**A**) Overlay of ^{1}H-^{15}N TROSY-HSQC spectra of apo (green) and Ca^{2+}-bound NTD (cyan) spectra shows that the two states have very different conformation and/or dynamics.

(**B**) The ^{1}H-^{15}N TROSY-HSQC spectra of 0.1 mM ^{15}N-labeled apo NTD mixed with 2 mM LDAO (red), 3 mM DPC (magenta) and 0.3 mM DDM (green). In all three cases, the drastically broadened NMR spectrum indicates either unfolding or aggregation of the NTD.

(**C**) The ^{1}H-^{15}N TROSY-HSQC spectra of the apo NTD in the absence (left) and presence (right) of empty liposome. The two spectra are essentially identical.

(**D**) The same spectra as in (C) recorded for Ca^{2+}-bound NTD, showing essentially no change in the presence of liposome.

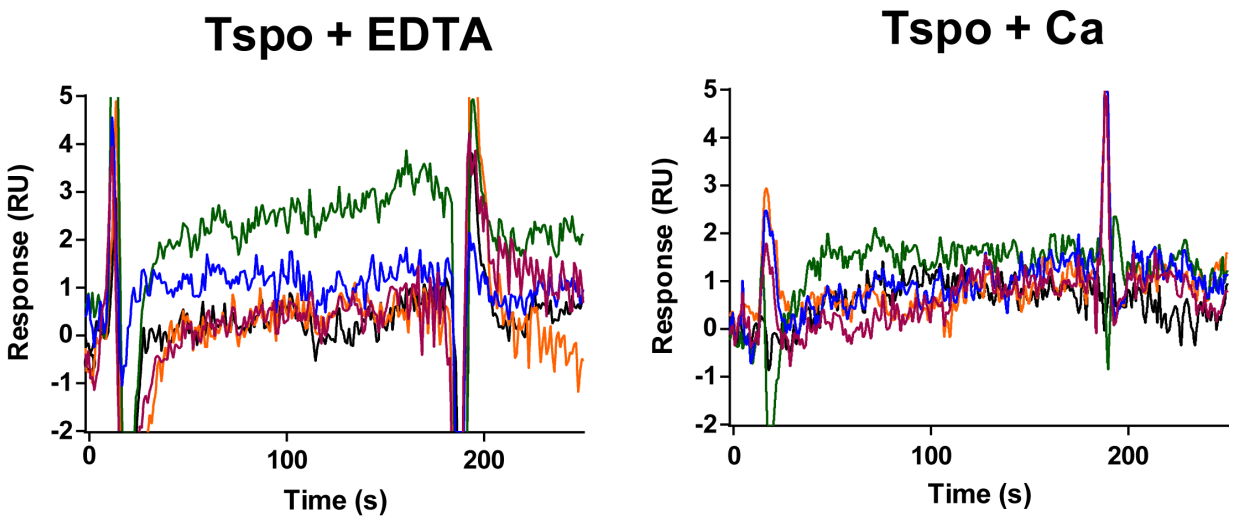

Figure S5. NTD does not binding to the Tryptophan-Rich Sensory Protein (TSPO), an 18 kDa bacterial homolog of the porphyrin binding protein in the outer membrane of mitochondria. SPR sensorgrams of the binding of NTD to immobilized TMD proteoliposomes at different NTD concentrations in the presence of 5mM EDTA (left) and 5 mM Ca^{2+} (right).

Supplemental Experimental Procedures

Sample preparation

For preparing the NTD samples, a gene encoding residues 1-193 of SCaMC-1 and a C-terminal 6His-tag was synthesized by GenScript and subsequently cloned into pET21a expression vector. The NTD was expressed in BL21 (DE3) cells (New England Biolabs). The cells were initially grown at 37 °C in either Luria Broth or M9 minimal media. After induction, the protein was expressed overnight at 20 °C. For NTD purification, the cells were lysed and the supernatant was passed through cobalt resin (Clontech) pre-equilibrated with 20 mM HEPES (pH 7.4), 150 mM NaCl and 5 mM imidazole. The resin was washed in the same buffer with 20 mM imidazole. The protein was eluted with 200 mM imidazole and then passed through a HiLoad 16/60 Superdex 75 size exclusion column (GE healthcare) in 20 mM HEPES (pH 7.0), 20 mM NaCl and 5 mM $CaCl_2$. The purified NTD fraction was in the Ca^{2+}-bound form. The apo form of NTD was obtained by extensive dialysis against 20 mM HEPES (pH 7.0), 20 mM NaCl, 20 mM EDTA, and 5 mM EGTA for 3 times (12 hours each), followed by final dialysis against 20 mM HEPES (pH 7.0), 20 mM NaCl and 5 mM EDTA.

For preparing the TMD samples, a gene encoding residues 185-477 and a C-terminal 6His-tag was synthesized by GenScript and cloned into pET21a expression vector. TMD was also expressed in BL21 (DE3) cells and purified using a protocol similar to that previously reported (Berardi et al., 2011). Briefly, after cell lysis, TMD was extracted from cell membrane by adding 1% DPC into the cell lysate. The solublized TMD was loaded on a Ni-NTA resin and eluted with 0.1% DPC and 300 mM imidazole. The protein was further purified on a Superdex S200 size exclusion column in 0.1% DPC, 20 mM HEPES (pH 7.4), and 150 mM NaCl.

Crystallization, data collection, and structure determination

The Ca^{2+}-bound NTD was crystallized by hanging-drop vapor diffusion by mixing 1 µl of 0.5 mM protein sample with the reservoir solution consisting of 50 mM Tris (pH 7.8), 2 M lithium sulfate, and 4% (w/v) PEG 400 at 20 °C. Complete multiple wavelength anomalous diffraction (MAD) datasets were collected at Advanced Photon Source at Argonne National Laboratory with one selenomethionine-labeled crystal. The crystal belongs to the space group $P6_222$ and diffracted to a maximum resolution of 2.9 Å. A second crystal form was obtained using 100 mM CHES (pH 9.1) and 20% PEG3350 as

crystallization solution. Complete X-ray diffraction data at 2.1 Å was recorded at 100 K at l = 1.5418 Å on an inhouse MAR345 detector (MAR Research) mounted on a Bruker AXS rotating anode generator. This crystal belongs to the space group $P3_121$. Data were processed using the HKL2000 suite of programs (Otwinowski and Minor, 1997). Attempts to crystallize NTD in the absence of Ca^{2+} were unsuccessful.

The NTD structure was solved by MAD with the $P6_222$ crystal dataset using the program Phenix.AutoSol (Adams et al., 2010). After density modification, 134 out of 193 residues were built using Phenix.AutoBuild (Adams et al., 2010). This model was subsequently used as a search model for molecular replacement of the $P3_121$ crystal using the program Phaser (McCoy et al., 2007). Further improvements of the model from the $P3_121$ crystal were made using the program COOT (Emsley et al., 2010), followed by iterative cycles of positional and B-factor refinement performed using the program Phenix.Refine (Adams et al., 2010). The overall quality of the structure was evaluated using MOLPROBITY (Chen et al., 2010). Data collection and refinement statistics are summarized in Table 1.

NMR spectroscopy

NMR experiments were performed at 30 °C on 600 MHz Bruker spectrometer equipped with cryogenic TXI probe, except for relaxation data, which were recorded at 750 MHz. Data processing and spectra analyses were performed using programs NMRPipe (Delaglio et al., 1995), CARA (Keller, 2004) and CcpNmr (Vranken et al., 2005). The sequence-specific assignments of backbone $^{1}H^{N}$, ^{15}N, $^{13}C^{\alpha}$, $^{13}C^{\beta}$, and $^{13}C'$ chemical shifts for the apo and Ca^{2+}-bound states of SCaMC were achieved with three pairs of triple-resonance experiments HNCA/HNCOCA, HNCACB/HNCOCACB and HNCO/HNCACO using a $^{2}H/^{15}N/^{13}C$-labeled NTD sample.

The ^{1}H-^{15}N RDCs ($^{1}D_{NH}$) of the Ca^{2+}-bound NTD were measured using ^{15}N-labeled protein weakly aligned in 12 mg/ml filamentous phage Pf1 (Asla Biotech). The $^{1}D_{NH}$ values were obtained from $^{1}J_{NH}$ / 2 and ($^{1}J_{NH}$ + $^{1}D_{NH}$) / 2, which were measured at 600 MHz by interleaving a regular gradient-enhanced HSQC and a gradient-selected TROSY, both acquired with 80 ms of ^{15}N evolution. The sign of $^{1}D_{NH}$ follows the convention that $|^{1}J_{NH} + {}^{1}D_{NH}| < 90$ Hz when $^{1}D_{NH}$ is positive. For fitting $^{1}D_{NH}$ to the crystal structure of the Ca^{2+}-bound NTD, hydrogen atoms were added to the crystal structure based on idealized molecular geometry using the program PyMOL. Fitting of $^{1}D_{NH}$ to structure was done by singular value

decomposition (Losonczi et al., 1999), using the program PALES (Zweckstetter and Bax, 2000). The goodness of fit was assessed by both Pearson correlation coefficient (*R*) and the quality factor (*Q*) (Cornilescu et al., 1998).

Dynamics measurements for apo and Ca^{2+}-bound NTD were performed at 30 °C and on 750 MHz Bruker spectrometer. ^{15}N R_1, R_2, and $^{15}N(^1H)$ NOE were measured using the standard pulse schemes described previously (Kay et al., 1989). The heteronuclear $^{15}N(^1H)$ NOE was measured by recording HSQC spectrum with and without 3 s duration of proton saturation in an interleaved manner. For ^{15}N R_1 measurement, relaxation delays of 0, 120, 240, 480, and 720 ms were used. For ^{15}N R_2 measurement, delays of 0, 10, 20, 40, 80, and 120 ms were used.

Proteoliposome binding measurements

Preparation of TMD proteoliposome. A lipid stock solution of POPC, POPG and Cardiolipin (4:1:0.1 molar ratio) was made by dissolving the lipids (Avanti) in 200 mM Fos-choline 10 (Anatrace), 20 mM HEPES (pH 7.0) and 150 mM NaCl to total lipid concentration of 50 mM. To prepare the TMD proteoliposomes, the lipid stock solution was added to the DPC-solubilized SCaMC-1 TMD at a 200:1 lipid:protein ratio, and then diluted with 20 mM HEPES (pH 7.0), 150 mM NaCl and 30 mM Fos-choline 10 to final lipid concentration of 40 mM for NMR titration or 0.5 mM for SPR experiments. Detergent was then removed by extensive dialysis (6 times, 12 hours each) against the respective NMR buffer or SPR running buffer (20 mM HEPES (pH 7.0), 150 mM NaCl and 5 mM EDTA), followed by two rounds of detergent clean up using Biobeads SM2 (Bio-rad). Proteoliposomes were extruded through 0.2 μM polycarbonate membranes (Whatman) 15 times. The final proteoliposome solution contained 40 mM total lipid and 0.2 mM TMD for NMR experiments, or 0.5 mM total lipid and 2.5 mM TMD for SPR experiments. Empty liposomes were prepared in the same way without the protein.

NMR measurements of NTD-TMD interaction. For NMR experiments, 0.2 mM ^{15}N-labeled NTD in the NMR buffer was mixed with equal volume of either TMD proteoliposome or empty liposome solution above. NMR readout was in the form of 2D gradient-selected TROSY HSQC spectra recorded at ^1H frequency of 600 MHz.

SPR measurements of NTD-TMD interaction. SPR experiments were performed with the Biacore 3000 instrument (GE healthcare) at 25 °C using a protocol similar to that described previously (Hodnik and

Anderluh, 2010; Stahelin, 2013). The experimental design involves 1) immobilizing the TMD proteoliposomes on the L1 sensor chip via interaction between the tail groups of lipids and the alkane groups present on the carboxymethyldextran-coated chip surface and 2) flowing NTD through the sensor chip in the absence and presence of Ca^{2+}. After the L1 sensor chip (GE healthcare) was washed with SPR running buffer (20 mM HEPES (pH 7.0), 150 mM NaCl, and 5 mM EDTA), TMD proteoliposomes or empty liposomes were injected at 10 µl/min for 15 minutes into active flow cell or control flow cell, respectively. The immobilized proteoliposomes were stabilized with injection of 20 µl of 2 M NaCl, followed by 10 µl of 0.1 mg/ml bovine serum albumin (BSA) (for saturating the non-specific binding sites). To measure binding, apo NTD in the SPR buffer with 0.1 mg/ml BSA was injected at increasing concentrations (1, 3, 10, 30, 100, 300 and 600 mM) at 2 µl/min for 3 minutes. The response in signal (RU) at each of the above protein concentration was recorded. Likewise, Ca^{2+}-bound NTD in HEPES (pH7.0), 150 mM NaCl, 0.1 mg/ml BSA and 5 mM $CaCl_2$ was injected at the same rate at concentrations of 9, 18.5, 37.5, 75, 150, 300 and 600 mM. The experiments were performed in triplicate. SPR data processing and analysis were performed using the program BIAevaluation (GE healthcare). Sensorgrams were corrected for changes in the refractive index of the buffer and non-specific binding by subtracting the response of the control channel with immobilized empty liposomes. Equilibrium signal (R_{eq}) at a given NTD concentration (C) were plotted and fit to the equation $R_{eq} = R_{max}/(1 + K_D/C)$ to determine the equilibrium binding constant (K_D). R_{max} is the binding signal at saturation.

References:

Adams, P.D., Afonine, P.V., Bunkoczi, G., Chen, V.B., Davis, I.W., Echols, N., Headd, J.J., Hung, L.W., Kapral, G.J., Grosse-Kunstleve, R.W.*, et al.* (2010). PHENIX: a comprehensive Python-based system for macromolecular structure solution. Acta Crystallogr D Biol Crystallogr *66*, 213-221.

Berardi, M.J., Shih, W.M., Harrison, S.C., and Chou, J.J. (2011). Mitochondrial uncoupling protein 2 structure determined by NMR molecular fragment searching. Nature *476*, 109-113.

Chen, V.B., Arendall, W.B., 3rd, Headd, J.J., Keedy, D.A., Immormino, R.M., Kapral, G.J., Murray, L.W., Richardson, J.S., and Richardson, D.C. (2010). MolProbity: all-atom structure validation for macromolecular crystallography. Acta Crystallogr D Biol Crystallogr *66*, 12-21.

Cornilescu, G., Marquardt, J.L., Ottiger, M., and Bax, A. (1998). Validation of protein structure from anisotropic carbonyl chemical shifts in a dilute liquid crystalline phase. J Am Chem Soc *120*, 6836-6837.

Delaglio, F., Grzesiek, S., Vuister, G.W., Zhu, G., Pfeifer, J., and Bax, A. (1995). NMRPipe: a multidimensional spectral processing system based on UNIX pipes. J Biomol NMR *6*, 277-293.

Emsley, P., Lohkamp, B., Scott, W.G., and Cowtan, K. (2010). Features and development of Coot. Acta Crystallogr D Biol Crystallogr *66*, 486-501.

Gouet, P., Courcelle, E., Stuart, D.I., and Metoz, F. (1999). ESPript: analysis of multiple sequence alignments in PostScript. Bioinformatics *15*, 305-308.

Goujon, M., McWilliam, H., Li, W., Valentin, F., Squizzato, S., Paern, J., and Lopez, R. (2010). A new bioinformatics analysis tools framework at EMBL-EBI. Nucleic Acids Res *38*, W695-699.

Hodnik, V., and Anderluh, G. (2010). Capture of intact liposomes on biacore sensor chips for protein-membrane interaction studies. Methods Mol Biol *627*, 201-211.

Jones, D.T. (1999). Protein secondary structure prediction based on position-specific scoring matrices. J Mol Biol *292*, 195-202.

Kay, L.E., Torchia, D.A., and Bax, A. (1989). Backbone dynamics of proteins as studied by 15N inverse detected heteronuclear NMR spectroscopy: application to staphylococcal nuclease. Biochemistry *28*, 8972-8979.

Keller, R. (2004). The computer aided resonance assignment tutorial. Goldau, Switzerland.

Losonczi, J.A., Andrec, M., Fischer, M.W., and Prestegard, J.H. (1999). Order matrix analysis of residual dipolar couplings using singular value decomposition. J Magn Reson *138*, 334-342.

McCoy, A.J., Grosse-Kunstleve, R.W., Adams, P.D., Winn, M.D., Storoni, L.C., and Read, R.J. (2007). Phaser crystallographic software. J Appl Crystallogr *40*, 658-674.

Otwinowski, Z., and Minor, W. (1997). Processing of X-ray Diffraction Data Collected in Oscillation Mode. In Macromolecular Crystallography, part A (Academic Press), pp. p.307-326.

Stahelin, R.V. (2013). Surface plasmon resonance: a useful technique for cell biologists to characterize biomolecular interactions. Molecular biology of the cell *24*, 883-886.

Vranken, W.F., Boucher, W., Stevens, T.J., Fogh, R.H., Pajon, A., Llinas, M., Ulrich, E.L., Markley, J.L., Ionides, J., and Laue, E.D. (2005). The CCPN data model for NMR spectroscopy: development of a software pipeline. Proteins *59*, 687-696.

Zweckstetter, M., and Bax, A. (2000). Prediction of sterically induced alignment in a dilute liquid crystalline phase: aid to protein structure determination by NMR. J Am Chem Soc *122*, 3791-3792.